

Article

The Fluid Evolution in the Skarn Stages of the Baoshan Skarn Cu-Polymetallic Deposit, South China

Ping Zheng¹, Ke Chen^{2,3,*}, Jun-Ke Zhang^{2,3}, Zhong-Fa Liu^{2,3}, Yong-Shun Li^{2,3} and Ming-Peng He^{2,3}¹ Department of Natural Resources, Hunan Vocational College of Engineering, Changsha 410151, China² Key Laboratory of Metallogenic Prediction of Nonferrous Metals and Geological Environment Monitoring, Central South University, Ministry of Education, Changsha 410083, China³ School of Geosciences and Info-Physics, Central South University, Changsha 410083, China

* Correspondence: chenke1026@csu.edu.cn

Abstract: Baoshan is a world-class skarn Cu-polymetallic deposit located at the junction of the Nanling and Qin-Hang metallogenic belts in China. While there has been extensive research on the mineralogy and geochemistry of skarn deposits, studies on the fluid characteristics and evolutionary history from the early to late skarn stages in such deposits are still limited. In this study, we analyzed garnet and pyroxene from the early skarn stage and scheelite from the late skarn stage of the Baoshan deposit. We distinguished two generations of garnet (Grt1 and Grt2), one generation of pyroxene, and three generations of scheelite (Sch I, Sch II, and Sch III) on the basis of mineral assemblages and microscopic characteristics. Grt1 appears coarse-grained, and Grt2 cuts through Grt1 as veinlets. In Grt1, the andradite end-member increases from the core to the rim, while the grossular portion decreases ($Ad_{35-36}Gr_{59-61}Sp_{3-4}$ to $Ad_{59-61}Gr_{36-37}Sp_{2-3}$), and in Grt2, the andradite end-member significantly increases ($Ad_{41-73}Gr_{25-55}Sp_{2-3}$). Grt1 and Grt2 have similar trace element compositions, with enrichment in Zr and depletion in Nb and Hf, depletion in LREE, enrichment in HREE, and weak negative Eu anomalies. Pyroxene coexists with Grt1 and is similarly cut by Grt2, with its composition mainly being diopside ($Di_{82-99}Hd_{0.6-15}Jo_{0-3.2}$). Sch I and Sch II appear as anhedral to subhedral grains, while Sch III is predominantly found in veinlets. In Sch I and Sch II, most REEs enter the scheelite lattice via the Na-REE coupled substitution mechanism, with a smaller portion substituting Ca vacancies. In Sch III, the substitution mechanism involving Ca site vacancies may dominate. During the early skarn stage, the oxygen fugacity of the fluid gradually decreased from Grt1 and pyroxene to Grt2. In the late skarn stage, fluid oxygen fugacity remains stable from Sch I and Sch II to Sch III in shallow parts but significantly decreases in deeper parts. The garnet and pyroxene from the Baoshan deposit align with typical skarn Cu deposit compositions, while scheelite in the late skarn stage shows Sch I, Sch II, and shallow Sch III as skarn-type and deep Sch III as vein-type scheelite. Early skarn stage fluids were weakly acidic. Sch I, Sch II, and Sch III originated from fluids related to the Baoshan granite porphyry, with Sch III also showing evidence of water-rock interaction. This study reconstructed the fluid evolution history from the early to late skarn stages at the Baoshan deposit, providing insights into the ore-forming processes of other skarn deposits.



Citation: Zheng, P.; Chen, K.; Zhang, J.-K.; Liu, Z.-F.; Li, Y.-S.; He, M.-P. The Fluid Evolution in the Skarn Stages of the Baoshan Skarn Cu-Polymetallic Deposit, South China. *Minerals* **2024**, *14*, 907. <https://doi.org/10.3390/min14090907>

Academic Editors: Ferenc Molnár and Pierfranco Lattanzi

Received: 4 July 2024

Revised: 24 August 2024

Accepted: 4 September 2024

Published: 5 September 2024

Keywords: major and trace elements; garnet; pyroxene; scheelite; Baoshan Cu-polymetallic deposit



Copyright: © 2024 by the authors. Licensee MDPI, Basel, Switzerland. This article is an open access article distributed under the terms and conditions of the Creative Commons Attribution (CC BY) license (<https://creativecommons.org/licenses/by/4.0/>).

1. Introduction

Scheelite ($CaWO_4$), one of the primary host minerals of tungsten (W), has a trace element composition that can effectively reflect hydrothermal conditions and the evolution process [1–5]. Meanwhile, scheelite is also a key mineral for fluid inclusion studies, providing direct evidence of hydrothermal fluids by indicating their temperature, salinity, pressure, and composition [6–8]. Moreover, isotope studies (e.g., Sr, Sm-Nd, and U-Pb) of scheelite are valuable for tracing the origin of metallogenic materials and determining the

mineralization timing [9–14]. Previous research suggests that the REE distribution in scheelite can be used to distinguish different types of deposits, indicating a genetic relationship between the trace element composition of scheelite and geological events [15,16].

Garnet is widely developed in pegmatite, granite, metamorphic rock, and skarn [17–19], and most garnets belong to a solid solution series of two or more end-member components [20,21]. In the skarn system, the geochemical composition of garnet is often used to reflect the physicochemical conditions of hydrothermal fluids or to reconstruct the fluid evolution history [22–24]. Pyroxene, as a common mineral in skarn-type deposits, is often used to determine deposit types and fluid characteristics [21].

The southern Hunan Province boasts exceptional mineralization conditions and is rich in metal resources such as W, Sn, Cu, Pb, and Zn. It is renowned as a major hub for non-ferrous metals in China. The region's prominent ore deposits include Sn polymetallic deposits like Xianghualing, Furong, and Hehuaping; W polymetallic deposits such as Shizhuyuan, Xintianling, Yaogangxian, and Weijia; and Cu-Pb-Zn polymetallic deposits including Tongshanling, Baoshan, Huangshaping, and Shuikoushan. Additionally, the Dafang Au deposit is notable. These deposits are closely associated with the Yanshanian magmatic hydrothermal activity in the area. As a representative Cu-polymetallic deposit in the region, extensive research has been conducted on the diagenetic and metallogenic ages, magma source areas and processes, and evolution of ore-forming fluids in the Baoshan deposit [25–33]. The fluid evolution history of skarn deposits is crucial for understanding the sources of metals and the mineralization processes in such deposits. Currently, few studies have analyzed the comprehensive fluid evolution history from the early to late skarn stages in skarn deposits. The Baoshan deposit, as a typical skarn deposit, provides a window into studying fluid evolution in skarn systems. Moreover, the widespread presence of garnet, pyroxene, and scheelite in the skarn stages suggests that geochemical studies of these minerals could provide insights into the fluid evolution during the formation of the skarn mineralization system.

In this study, on the basis of detailed geological surveys and microscopic observations, we systematically analyze the major and trace element geochemical characteristics of garnet and pyroxene in the early skarn stage and scheelite in the late skarn stage of the Baoshan Cu-polymetallic deposit using cathodoluminescence (CL), electron probe microanalysis (EPMA), and laser ablation inductively coupled plasma mass spectrometry (LA-ICP-MS) techniques to determine the substitution mechanism of rare earth elements in scheelite and the characteristics and evolution history of fluids, especially the transition of fluids from the early to late skarn stage. This helps us understand the role of fluid characteristics and evolution in the mineralization of skarn deposits.

2. Geological Setting

2.1. Regional Geology

The southern Hunan ore concentration area, part of the South China metallogenic domain, is situated within the late Proterozoic collisional contact zone between the Yangtze and Cathaysia blocks (Figure 1) [34]. It is also located at the intersection of the east-west-trending Nanling W-Sn polymetallic metallogenic belt and the northeast-trending Qin-Hang Cu-Pb-Zn polymetallic metallogenic belt in South China, giving it a unique tectonic and dynamic background. Since the Paleozoic era, the southern Hunan Province has experienced complex tectonic and magmatic activities. The Caledonian orogeny caused the metamorphism of Cambrian–Sinian sedimentary rocks and the uplift of basement folds. Devonian–Permian carbonate rocks underwent significant folding. Jurassic–Cretaceous tectonic activity resulted in the formation of northeast-trending rift-related basins and major faults [35].

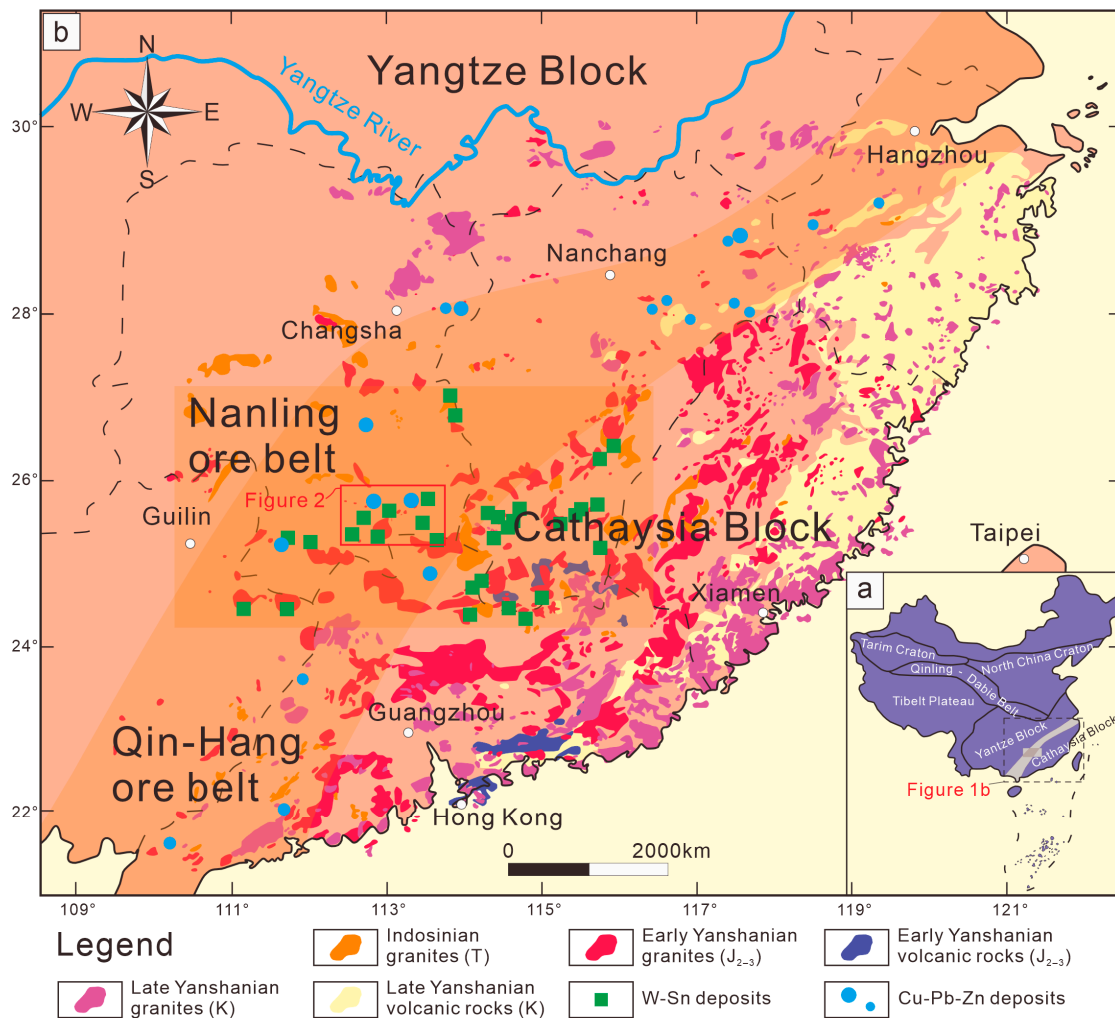


Figure 1. (a) Sketch map of the regional tectonic framework. (b) Distributions of the Jurassic granites and deposits in the South China Block. Modified from Zhou et al. [36].

The strata in the southern Hunan Province are relatively complete. Except for the Ordovician and Silurian periods, all strata from the Sinian to the Quaternary are exposed (Figure 2). Among these strata, the Paleozoic carbonate rocks are the most significant ore-bearing layers in the area, predominantly controlling the mineralization pattern, which is primarily characterized by skarn-type mineralization [37,38]. Influenced by the collision and orogeny of the Tethys Indosinian block, the North China block, and the South China block, a series of NNE-trending thrust nappe structures formed during the Indosinian period, establishing the main tectonic framework of this area [39–41]. Under the influence of Paleo-Pacific subduction and north–south landmass extrusion, a series of NE-trending thrust nappe structures developed during the Yanshanian period [42,43]. During the extensional setting of the Middle–Late Jurassic, intense magmatic activity led to the formation of extensive post-collision granites, which were accompanied by significant mineralization [44–47]. Since the convergence of the Neoproterozoic Yangtze Block and Cathaysia Block, this area has experienced several stages of tectonic–magmatic activity. The Yanshanian stage was the most intense and is most closely associated with mineralization, primarily controlled by NE-trending structures [37]. The genetic types of W-Sn deposits in this area are complex, encompassing porphyry, greisen, altered granite, skarn, quartz vein, and cassiterite sulfide types. The Cu-Pb-Zn polymetallic deposits are predominantly skarn-type and hydrothermal vein-type.

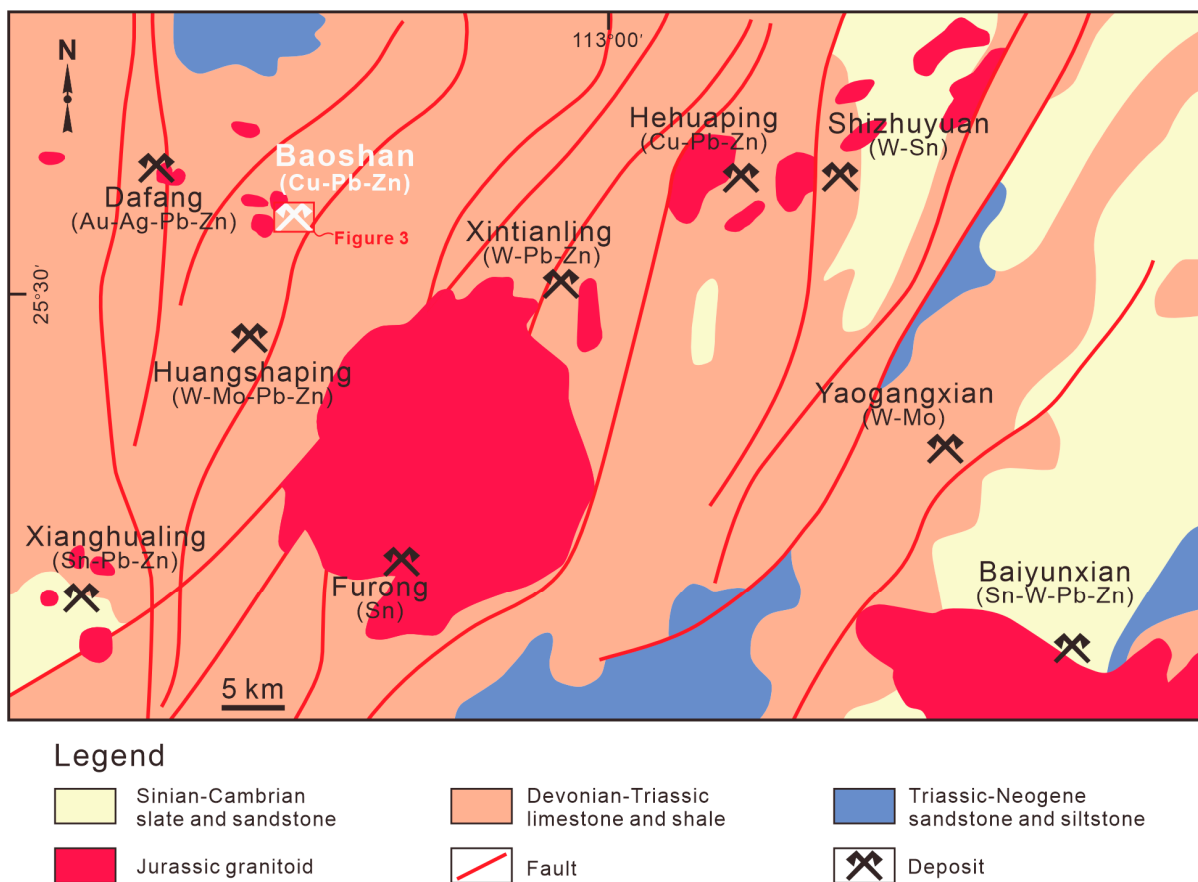


Figure 2. Sketch map of the regional geology showing the tectonic framework and mineralization resources. Modified from Li et al. [43].

2.2. Deposit Geology

The Baoshan deposit is located at the intersection of the Qin-Hang and Nanling ore belts, with estimated total resources of 0.24 Mt Cu at a grade of 1.28%, 0.47 Mt Pb at 3.82%, 0.51 Mt Zn at 4.34%, and 0.012 Mt Mo [25]. The exposed lithology associated with the Baoshan deposit consists predominantly of neritic marine sediments. These include the Upper Devonian Xikuangshan Formation, the Lower Carboniferous Menggong'ao, Shidengzi, Ceshui, and Zimenqiao Formations, as well as the Middle-Upper Carboniferous Hutian Group (Figure 3). The area is characterized by NE-trending thrust nappe faults and closed inverted folds, which developed in response to the subduction of the Paleo-Pacific plate. Additionally, these structures have been intersected by three NW-trending strike-slip faults at the Baoshan deposit. Intense magmatism is observed at the Baoshan deposit, which includes granite porphyry (180.5 ± 1.6 Ma) [35], granodioritic cryptoexplosive breccias (157 ± 1.8 Ma) [37], and lamprophyres (156 ± 2 Ma) [48]. Additionally, granodiorite porphyry formed between 162 and 155 Ma [31,35,37,38,43,49]. This timing aligns with the mineralization age indicated by molybdenite Re-Os dating at 160 ± 2 Ma [49] and grossular-rich garnet U-Pb dating at 162.6 ± 2.9 Ma [43]. As a representative Cu-polymetallic deposit, the Cu skarn mineralization is hosted within the limestone of the Shidengzi Formation and is controlled by the NE-trending Baoling inversion anticline in the central mining district. In contrast, the Pb-Zn hydrothermal vein-type mineralization primarily occurs in the dolomite of the Zimenqiao Formation along faults, predominantly located in the eastern, western, and northern mining districts [50]. The Baoshan deposit exhibits intense hydrothermal alteration, mainly including potassic alteration, silicification, sericitization, skarnization, carbonatization, and fluoritization, among which skarnization, silicification, fluoritization, and carbonatization are most closely related to mineralization (Figure 4).

The minerals in these hydrothermal alteration zones are quite complex, including garnet, diopside, epidote, chlorite, actinolite, quartz, fluorite, and sericite. Potassic alteration, epidotization, sericitization, and silicification are commonly found in the ore-forming granodiorite porphyry (Figure 4a); skarnization and silicification are closely associated with Cu and Mo mineralization (Figure 4b).

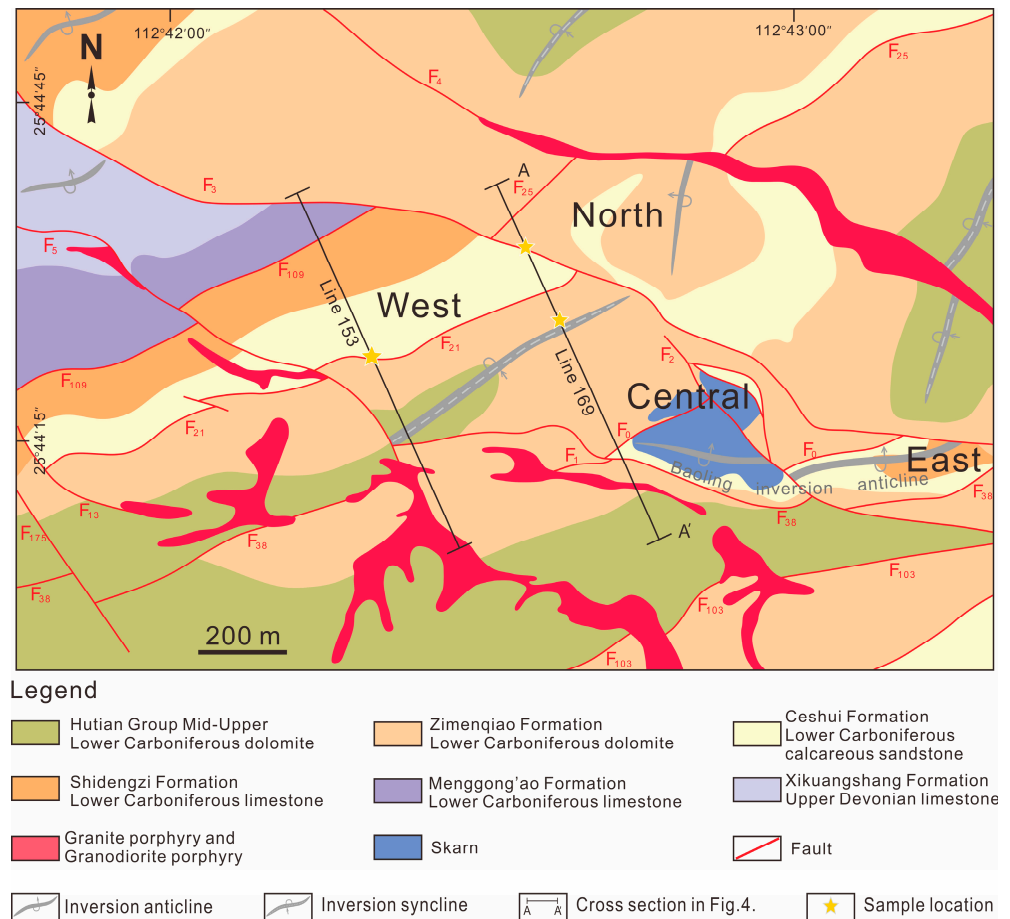


Figure 3. Simplified geologic map of the Baoshan Cu-polymetallic deposit. After Zhang et al. [32].

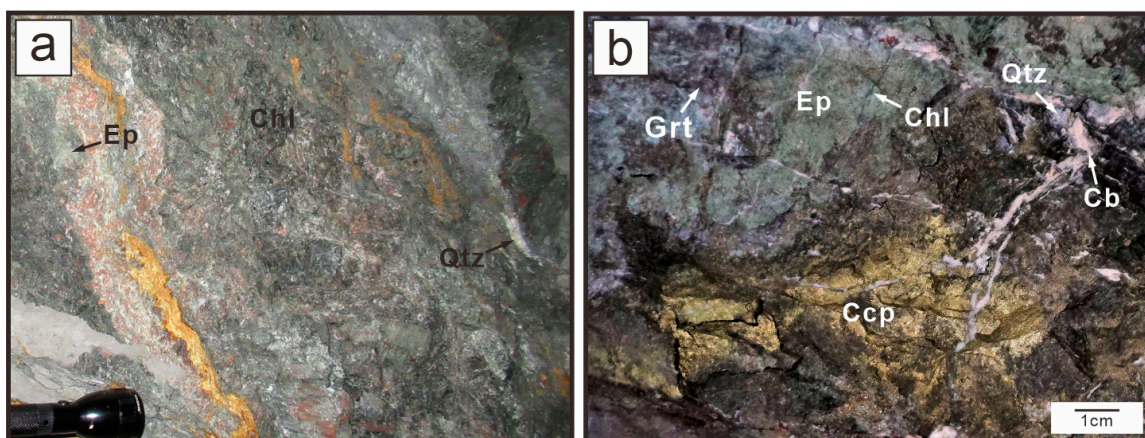


Figure 4. Hydrothermal alteration characteristics of the Baoshan deposit. (a) Development of potassic alteration, epidotization, chloritization, and silicification in the ore-forming granodiorite porphyry. (b) Skarnization and silicification are closely associated with Cu mineralization. Ep = epidote; Qtz = quartz; Chl = chlorite; Ccp = chalcopyrite; Grt = garnet; Cb = carbonate minerals.

3. Sampling and Analytical Methods

3.1. Sampling

On the basis of detailed geological surveys and systematic observations of various samples from the mining area, this study selects representative samples from each mineralization stage of the Baoshan deposit, specifically garnet and pyroxene from the early skarn stage and scheelite from the late skarn stage. The samples were systematically polished into thin sections. Combined with the results of microscopic petrographic identification, representative samples were selected for major and trace element analysis. Two representative samples from the skarn zone were taken from the 50 m and −190 m levels of Line 169 (S-50-169-1 and S-190-169-1) for garnet major and trace element analysis and pyroxene major element analysis (Figure 3). Three representative scheelite-bearing samples were collected from the Baoshan deposit for scheelite trace element analysis. Two samples are from the 50 m and −190 m levels of Line 169 (S-50-169-2 and S-190-169-2), which is the most significant exploration profile of the Baoshan deposit (Figure 5). The other one is collected from the 50 m level of Line 153 (S-50-153-2) for comparison. Standard polished thin sections (~30 μm) of each sample were prepared for EPMA and LA-ICP-MS analysis. Then, 100 μm to 500 μm size of scheelite grains were separated from the ores for cathodoluminescence imaging.

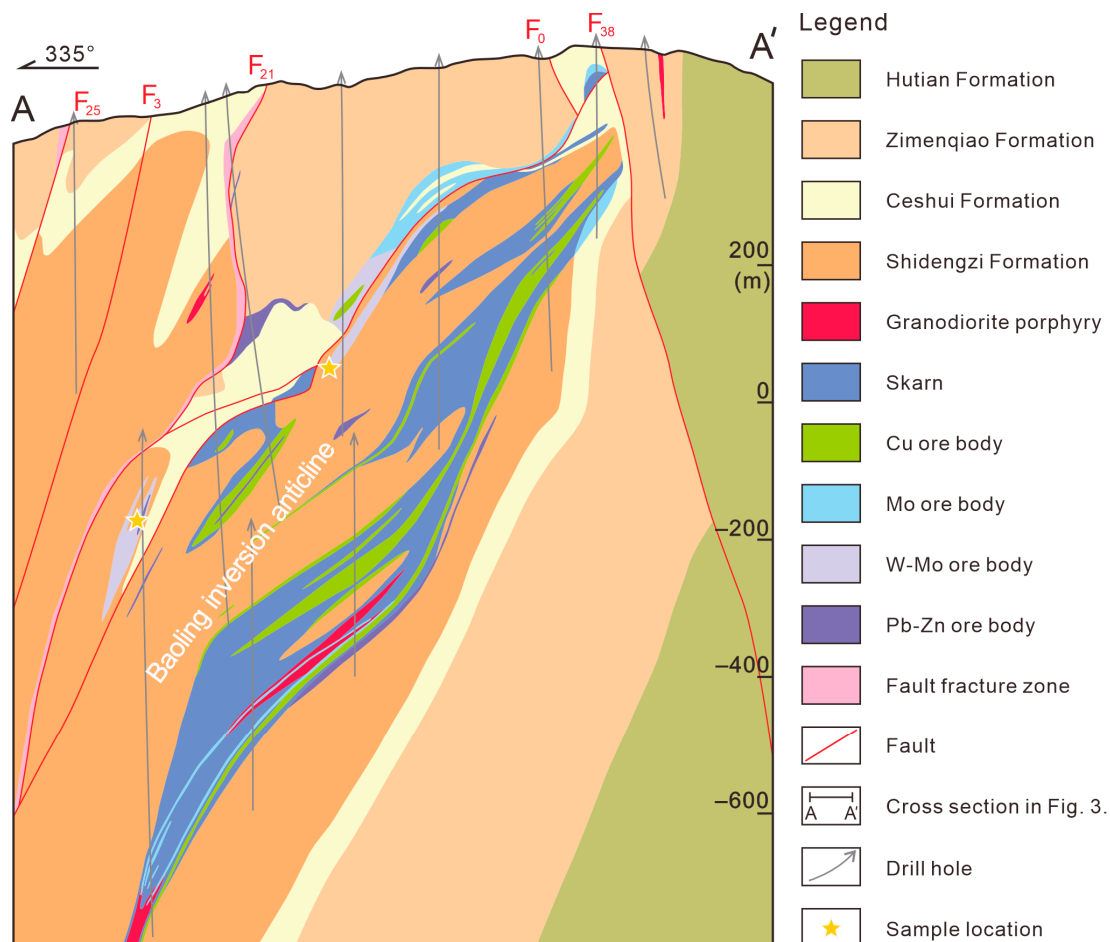


Figure 5. Cross section along the No. 169 prospecting line from the Baoshan Cu-polymetallic deposit. After Li et al. [51].

3.2. Analytical Methods

EPMA analysis, including quantitative energy dispersive spectroscopy (EDS), in situ major element analysis, and back-scattered electron (BSE) observations, were performed

at the School of Geosciences and Info-Physics (Central South University) on a Shimadzu EPMA-1720. The analytical parameters include a 15 kV accelerating voltage, 2.0×10^{-8} A probe current, 5 μm spot size, and 0.01% detection limit.

The cathodoluminescence imaging of the garnet and scheelite was conducted via a CAMECA cathodoluminoscope at 10 kV and 20 nA at the Guangzhou Touyan Analytical Technology Co., Ltd., China. Then, trace elements of scheelite were measured by use of an NWR 193 nm laser ablation system at the same place. The ion-signal intensities were collected by an iCAP RQ inductively coupled plasma mass instrument. The sealed ablation cell where the samples were placed was constantly flushed with pure Helium gas (~ 1.5 L/min). The laser beam size, energy, and repetition rate were 30 μm , 3 J/cm², and 6 Hz, respectively. Each analysis comprised a 30 s measurement of background acquisition, 40 s analysis for the sample, and 20 s washout time. The following isotopes were monitored: ²³Na₂O, ⁷¹Ga, ⁸⁵Rb, ⁸⁸Sr, ⁸⁹Y, ⁹¹Zr, ⁹³Nb, ⁹⁷Mo, ¹³⁵Ba, ¹³⁹La, ¹⁴⁰Ce, ¹⁴¹Pr, ¹⁴⁶Nd, ¹⁴⁷Sm, ¹⁵¹Eu, ¹⁵⁷Gd, ¹⁵⁹Tb, ¹⁶¹Dy, ¹⁶⁵Ho, ¹⁶⁶Er, ¹⁶⁹Tm, ¹⁷²Yb, ¹⁷⁵Lu, ¹⁸¹Ta, ²⁰⁸Pb, ²³²Th, and ²³⁸U. The standard sample was Glass NIST SRM610 with Ca as the internal standard, and SRM612 as the system monitoring sample [52]. The ICPMSDataCal was used to perform off-line selection and integration of background and analyzed signals and trace element analysis [53].

4. Results

4.1. Petrography and Cathodoluminescence (CL)

The detailed mineral paragenesis is presented in Figure 6. Garnet and diopside are typical minerals of the early skarn stage of the Baoshan deposit. On the basis of field geological intercalation relationships and micro-petrographic characteristics, the garnet in the Baoshan deposit is divided into two generations (Figure 7a). The early generation garnet (Grt1) is brown-red, with a coarse-grained granular structure (Figure 7b). It exhibits mostly total extinction under crossed polarizers with weak heterogeneity. It is often replaced by minerals such as diopside, epidote, actinolite, quartz, calcite, and late sulfides. The late generation garnet (Grt2) appears as dark brown veinlets, cutting through and replacing the early garnet and pyroxene (Figure 7a,c). Under the microscope, it appears yellow-brown, with a subhedral–anhedral structure and total extinction.

In the Baoshan deposit, the diopside does not show obvious multi-generation characteristics in the field. It appears gray-green, often replacing Grt1 in a bay-shaped manner and then being cut by Grt2 (Figure 7d). Under the microscope, it is colorless to yellow-green, with obvious pleochroism and a subhedral short-columnar to granular structure. It is often replaced by late-stage carbonate minerals.

Scheelite appears in subhedral to anhedral grains (20–400 μm) and is predominantly found in skarn and sulfide ores, exhibiting a disseminated appearance. It commonly coexists with garnet, epidote, chlorite, pyrite, and magnetite (Figure 8a–c). No obvious zonation in structure or composition is visible under transmitted or reflected light (Figure 8d–f). On the basis of mineral cutting relationships, it can be inferred that scheelite crystallized after garnet (Figure 8a) but before the formation of retrograde skarn minerals (e.g., epidote and chlorite; Figure 8d), as well as magnetite and sulfides (Figure 8e,f).

However, the cathodoluminescence (CL) images of scheelite shown in Figure 9 reveal a different story. Three generations of scheelite are identified from the Baoshan deposit. Scheelite I (Sch I) appears as euhedral to subhedral grains with oscillating bands and a relatively CL-dark appearance (Figure 9a–d). Scheelite II (Sch II) generally has a homogeneous CL intensity and replaces Sch I (Figure 9a–c). Sch II can be easily distinguished from Sch I by the absence of oscillating bands and its relatively CL-bright in appearance (Figure 9b). Unlike Sch I and Sch II, Scheelite III (Sch III) predominantly exhibits a veinlet appearance with the darkest color in the CL images and inhomogeneous CL intensity (Figure 9c,d). Representative scheelite grains and the locations of LA-ICP-MS measurements in three samples are presented (Figure 9e–g).

Stage Mineral	Early skarn stage (S ₁)	Late skarn stage (S ₂)	Cu-Fe sulfide stage (S ₃)	Pb-Zn sulfide stage (S ₄)
Wollastonite	-----			
Garnet	<u>Gr_{t1}</u> <u>Gr_{t2}</u>			
Diopside	<u>-----</u>			
Epidote				
Tremolite			
Actinolite			
Chlorite		-----		
Scheelite		<u>Sch I</u> <u>Sch II</u> <u>Sch III</u>		
Quartz		-----		
Magnetite		-----		
Pyrite		-----	-----	
Calcite			-----	
Chalcopyrite			-----	
Native gold			
Molybdenite			-----	
Sphalerite			-----	
Tetrahedrite			-----	
Arsenopyrite			
Galena				-----
Fluorite				-----

Figure 6. Mineral paragenesis of Baoshan deposit.

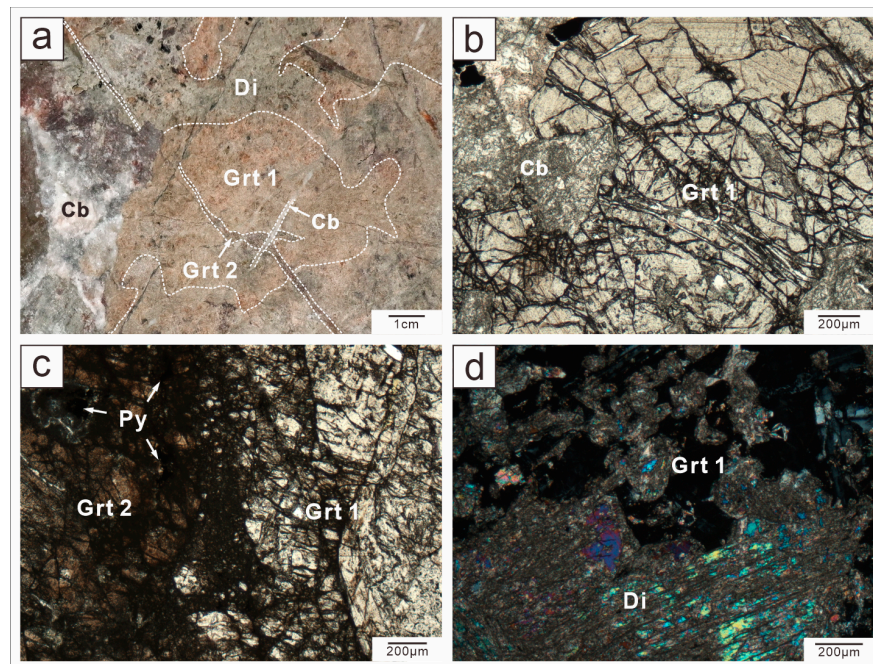


Figure 7. Macroscopic and microscopic features of the two generations of garnet and pyroxene in the Baoshan deposit. (a) Replacement and cross-cutting relationship between diopside and garnet. (b) Grt1 develops a coarse-grained granular structure (–). (c) Grt2 replaces Grt1; transmitted light (–). (d) Diopside replacing Grt1 in a bay-shaped pattern; transmitted light (+). Grt = garnet; Di = diopside; Cb = carbonate minerals; Py = pyrite.

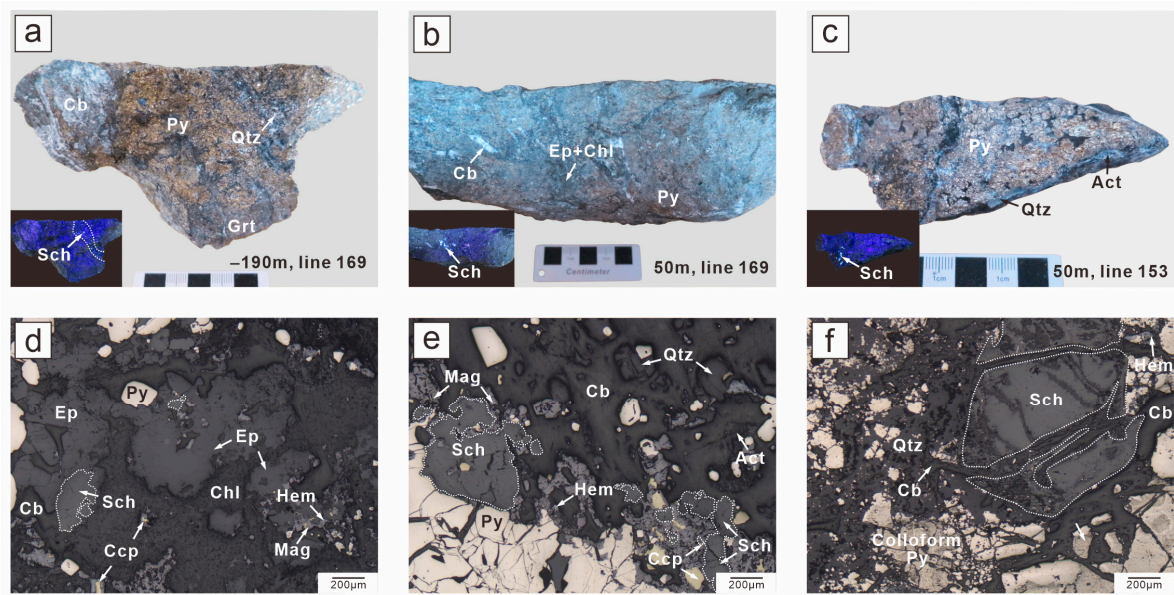


Figure 8. Three representative samples of scheelite from the Baoshan deposit. (a) Scheelite-bearing quartz veinlet cut the garnet skarn. (b) Scheelite in the skarn-hosted ores coexisting with retrograde minerals (epidote and chlorite). (c) Disseminated scheelite in the sulfide ores. (d) Scheelite has been replaced by epidote and chlorite; reflected light. (e) Scheelite exhibits an island appearance, cut by pyrite and magnetite; reflected light. (f) Coarse-grained scheelite coexists with the latter colloform pyrite and is altered along the fractures. Sch = scheelite; Py = pyrite; Grt = garnet; Qtz = quartz; Cb = carbonate; Ep = epidote; Chl = chlorite; Act = actinolite; Hem = hematite; Mag = magnetite; Ccp = chalcopyrite.

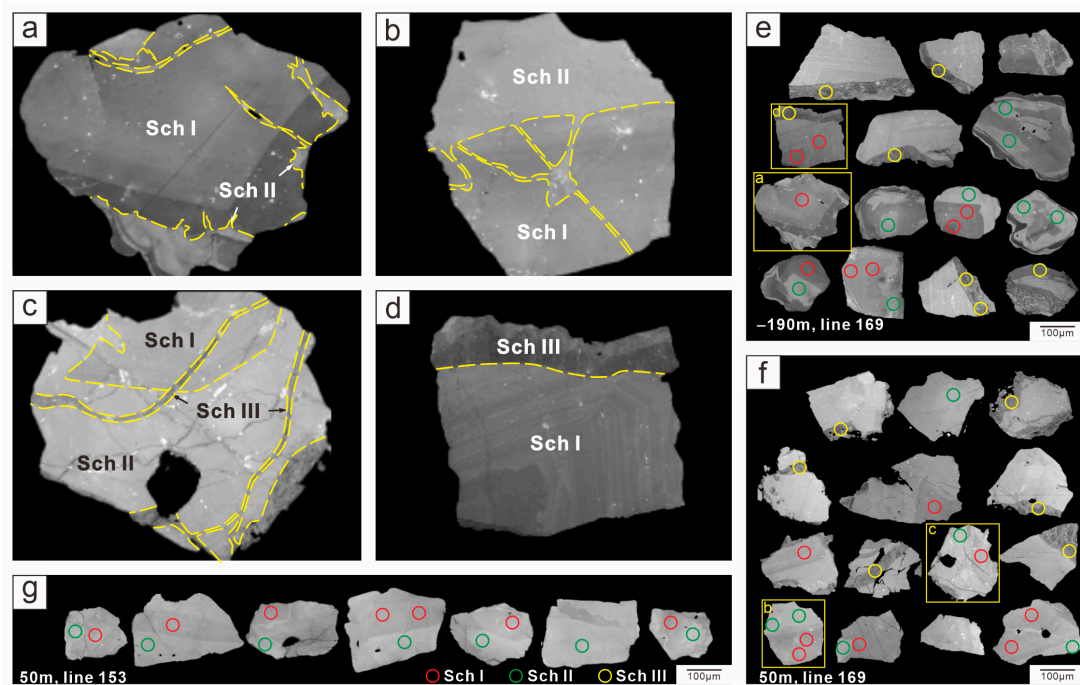


Figure 9. CL images of scheelite from the Baoshan deposit showing three generations and locations for the LA-ICP-MS. (a,b) Sch I and Sch II. (c) Sch I, Sch II, and Sch III. (d) Sch I and Sch III. (e) Scheelite from the -190 m levels of Line 169. (f) Scheelite from the 50 m levels of Line 169. (g) Scheelite from the 50 m levels of Line 153.

4.2. Major and Trace Element Geochemistry of Garnet

The major element analysis results of garnet (Supplementary Materials S1) show that in Grt1, the SiO₂ content ranges from 35.62 to 40.43 wt. %, with an average of 38.08 wt. %; TiO₂ content ranges from 0.17 to 0.41 wt. %, with an average of 0.33 wt. %; Al₂O₃ content ranges from 6.70 to 11.60 wt. %, with an average of 9.232 wt. %; FeO_T content ranges from 12.76 to 20.97 wt. %, with an average of 16.48 wt. %; MnO content ranges from 0.74 to 1.57 wt. %, with an average of 1.10 wt. %; MgO content ranges from 0.07 to 0.28 wt. %, with an average of 0.13 wt. %; and CaO content ranges from 30.52 to 32.49 wt. %, with an average of 31.55 wt. %. In Grt1, the andradite end-member proportion increases from the core to the rim, while the grossular end-member proportion gradually decreases (Ad_{35–36}Gr_{59–61}Sp_{3–4}–Ad_{59–61}Gr_{36–37}Sp_{2–3}) (Figure 10a). In Grt2, the SiO₂ content ranges from 40.49 to 42.89 wt. %, with an average of 41.99 wt. %; TiO₂ content ranges from 0.05 to 0.51 wt. %, with an average of 0.24 wt. %; Al₂O₃ content ranges from 3.97 to 9.14 wt. %, with an average of 5.52 wt. %; FeO_T content ranges from 14.12 to 23.36 wt. %, with an average of 19.74 wt. %; MnO content ranges from 0.53 to 0.98 wt. %, with an average of 0.70 wt. %; MgO content ranges from 0.06 to 0.18 wt. %, with an average of 0.11 wt. %; and CaO content ranges from 28.27 to 30.24 wt. %, with an average of 29.10 wt. %. Compared to Grt1, the proportion of andradite end-member in Grt2 significantly increases (Ad_{41–73}Gr_{25–55}Sp_{2–3}) (Figure 10a).

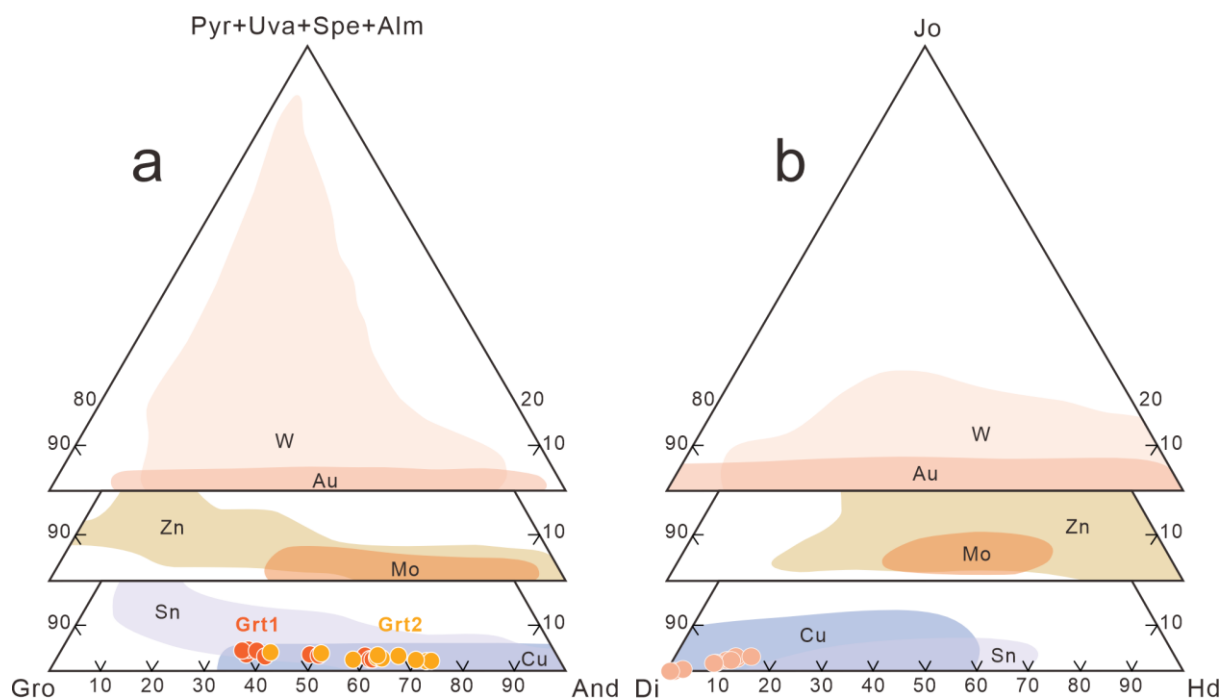


Figure 10. Triangular diagrams of garnet (a) and pyroxene (b) end-member compositions in the Baoshan deposit. The Au, Cu, Zn, Sn, W, and Mo skarn deposit fields are from Meinert et al. [54]. Pyr = Pyrope; Spe = Spessartine; Alm = Almandine; Uva = Uvarovite; Gro = Grossular; And = Andradite; Jo = Johannsenite; Di = Diopside; Hd = Hedenbergite.

The trace element analysis of garnet (Supplementary Materials S2) shows that Grt1 and Grt2 have similar trace element compositions, characterized by enrichment in Zr and depletion in Nb and Hf. The Zr, Nb, and Hf contents in Grt1 and Grt2 are 113.7–274.8 ppm and 59–213 ppm, 1.9–6.6 ppm and 7.6–15.6 ppm, and 2.5–6.7 ppm and 1.2–6.4 ppm, respectively. The Σ REE contents are 27.4–69.8 ppm and 30.8–59.8 ppm, both showing enrichment in LREE and depletion in HREE (LREE/HREE = 1.6–5.4 and 2.1–5.3) (Figure 11a,b), with weak negative Eu anomalies.

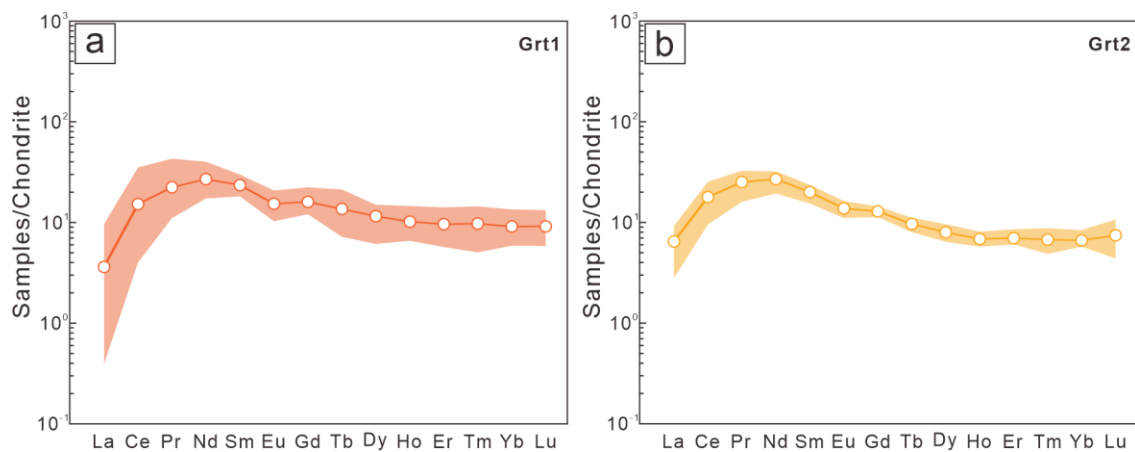


Figure 11. REE distribution pattern of Grt1 (a) and Grt2 (b) from the Baoshan deposit, chondrite-normalized according to the literature [55].

4.3. Major Element Geochemistry of Diopside

The major element analysis results of pyroxene from the Baoshan deposit (Supplementary Materials S3) show that the SiO₂ content ranges from 53.60 to 56.14 wt. %, with an average of 54.75 wt. %; Al₂O₃ content ranges from 0.12 to 1.72 wt. %, with an average of 0.57 wt. %; FeO content ranges from 0.19 to 4.77 wt. %, with an average of 2.71 wt. %; MgO content ranges from 15.00 to 18.33 wt. %, with an average of 16.46 wt. %; and CaO content ranges from 23.67 to 24.53 wt. %, with an average of 24.20 wt. %. The composition of pyroxene in Baoshan is mainly diopside (Di_{82–99}Hd_{0.6–15}Jo_{0–3.2}) (Figure 10b).

4.4. Trace Element Geochemistry of Scheelite

The trace element compositions of the three generations of scheelite from the representative samples are summarized in Supplementary Materials S4. Mo, Sr, and Y are highlighted in Figure 12 due to the significant variance in their concentrations among the different scheelite types.

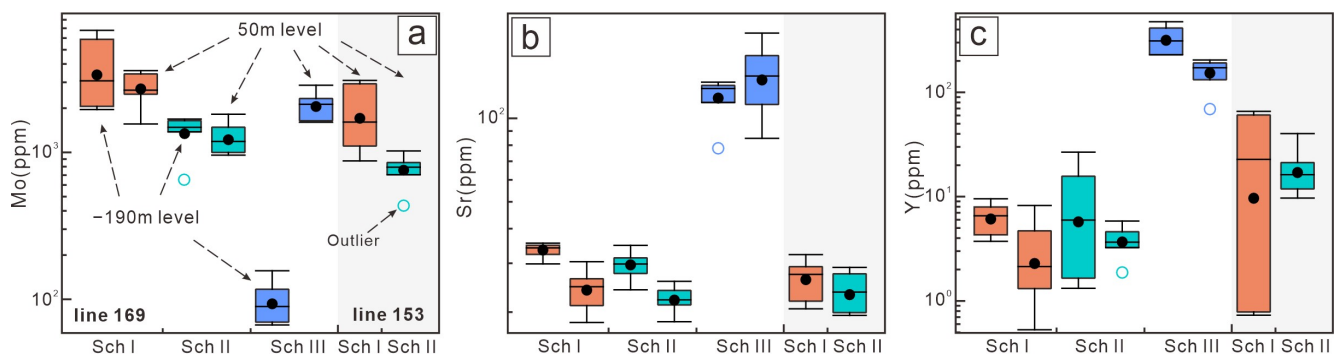


Figure 12. Plot of Mo (a), Sr (b), and Y (c) contents of scheelite from the Baoshan deposit, grouped into three generations.

The trace element analyses included 21 spots for Sch I (6 from S-190-169-2, 8 from S-50-169-2, and 7 from S-50-153-2), 21 spots for Sch II (7 from S-190-169-2, 7 from S-50-169-2, and 7 from S-50-153-2), and 13 spots for Sch III (7 from S-190-169-2 and 6 from S-50-169-2), resulting in a total of 55 corresponding LA-ICP-MS analyses.

Overall, the trace element composition in scheelite is generally consistent across the different exploration lines (Lines 169 and 153). Sr shows a fluctuating evolution from Sch I to Sch II to Sch III, whereas other elements exhibit either increasing (Y and Ba) or decreasing (Nb and Mo) trends. The highest concentrations of Sr and Y and the lowest concentrations

of Nb and Mo appear in Sch III. In general, the trace element concentration of scheelite does not vary significantly with depth, except for Mo, which breaks this pattern in Sch III.

5. Discussion

5.1. REE Pattern and Substitution Mechanism

Three primary substitution mechanisms for the incorporation of REE(+Y) into the crystal lattice of scheelite have been identified [56]: (1) $2\text{Ca}^{2+} = \text{REE}^{3+} + \text{Na}^+$; (2) $\text{Ca}^{2+} + \text{W}^{6+} = \text{REE}^{3+} + \text{Nb}^{5+}$; and (3) $3\text{Ca}^{2+} = 2\text{REE}^{3+} + \square_{\text{Ca}}$ (Ca site vacancy). At the Baoshan deposit, two primary REE patterns in scheelite have been observed: right-dip and hump-shaped (Figure 13). Sch I and Sch II exhibit high LREE/HREE ratios and a slight negative Eu anomaly (Figure 13a,b,d). In contrast, Sch III is characterized by high total REE concentrations, with the hump center between Sm and Gd, and either a positive or negative Eu anomaly (Figure 13c). These patterns suggest the presence of two distinct REE substitution mechanisms.

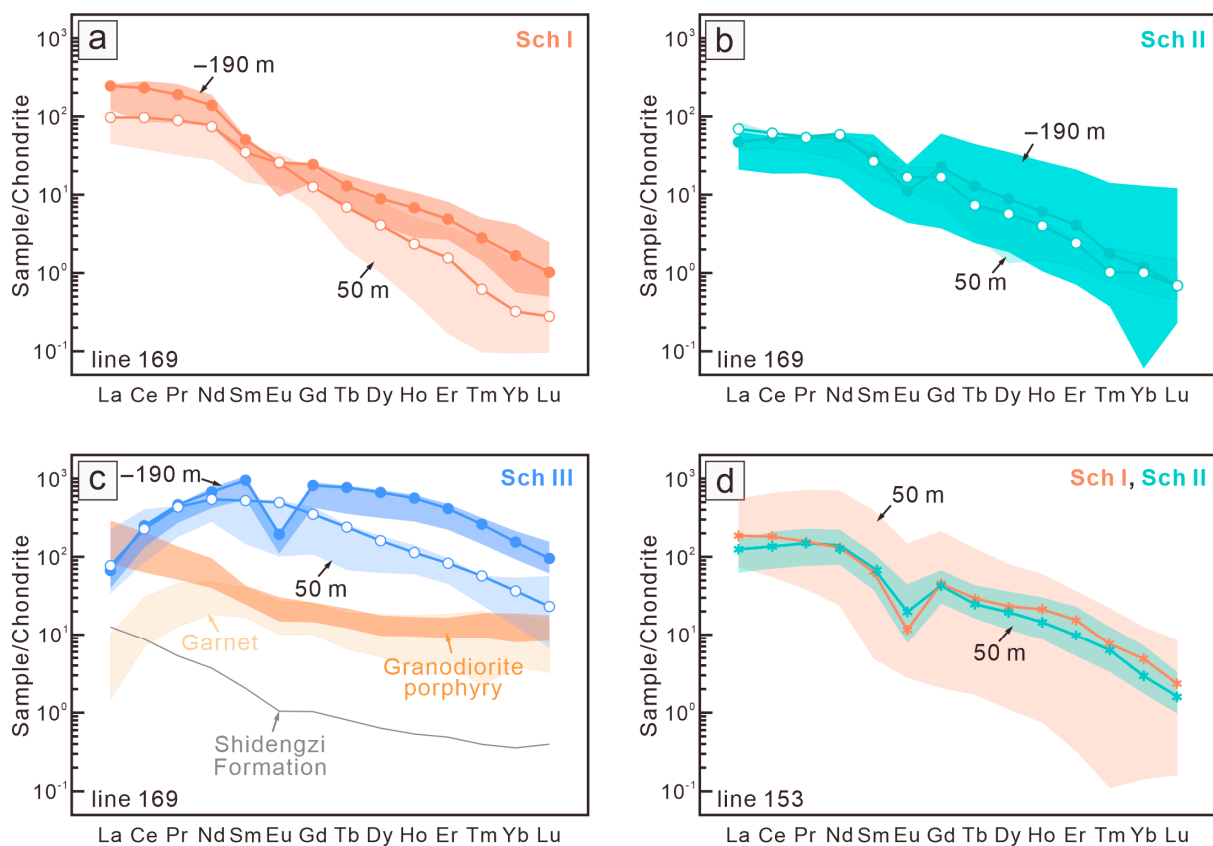


Figure 13. Chondrite-normalized REE patterns of Sch I from Line 169 (a), Sch II from Line 169 (b), Sch III from Line 169 (c), and Sch I + Sch II from Line 153 (d) from the Baoshan deposit. The chondrite-normalized REE patterns of granodiorite porphyry, garnet, and limestone of the Shidengzi Formation are also shown for comparison [31,35,37,38,57].

Most spots of Sch I and Sch II fall near the 1:1 correlation line, with Na increasing alongside $\sum\text{REE} + \text{Y-Eu}$ (Figure 14a). This suggests a Na-REE coupled substitution mechanism. However, a few spots deviate from this line, indicating that REEs might enter the scheelite lattice via the replacement of Ca site vacancies. The insufficient concentration of Na (average 13.5 ppm) and the weak correlation between Na and $\sum\text{REE} + \text{Y-Eu}$ (Figure 14) [2] suggest that the Ca site vacancy substitution mechanism may be dominant. Sch III falls far below the 1:1 correlation line, further indicating the Ca site vacancy mechanism (Figure 14a). Figure 14b also supports this, showing low Nb and high $\sum\text{REE} + \text{Y-Eu}$ concentrations across the three generations of scheelite. In this case, REEs of any size can

enter the scheelite lattice in pairs without preference. Given the weak influence of other factors on the REE pattern [56], the REE pattern in scheelite from the Baoshan deposit likely reflects the composition of the ore-forming fluid during its precipitation [58].

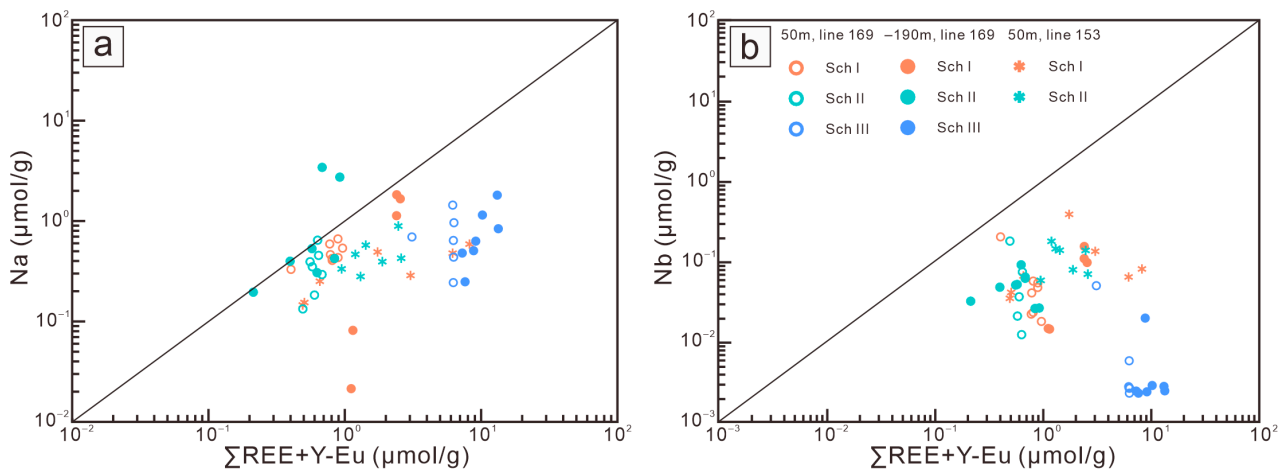


Figure 14. (a) Na and (b) Nb vs. $\Sigma\text{REE} + \text{Y-Eu}$ diagram for three generations of scheelite from the Baoshan deposit.

5.2. Redox State of Ore-Forming Fluids

The composition of pyroxene in Baoshan is predominantly diopside, indicating that the mineralizing hydrothermal fluids during the early skarn stage were generally under high oxygen fugacity conditions [59]. Additionally, changes in the U content in garnet can indicate variations in the oxygen fugacity of the mineralizing fluids, as low oxygen fugacity conditions tend to increase the U content in garnet [60,61]. The U content in Grt1 shows an increasing trend from the core to the rim; in Grt2, the U content is significantly higher than in Grt1 (Figure 15). This indicates that the oxygen fugacity of the mineralizing fluids during the early skarn stage gradually decreased.

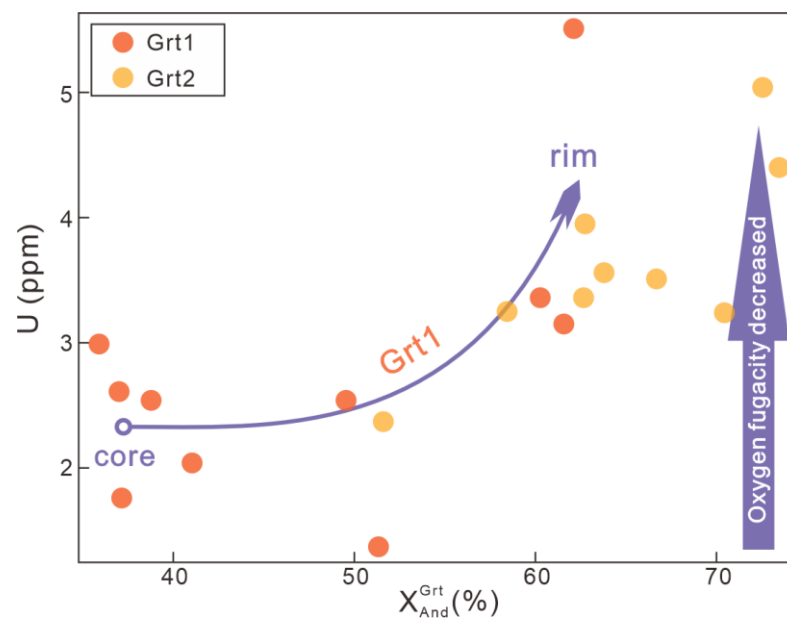


Figure 15. U vs. $X_{\text{And}}^{\text{Grt}}$ diagram of garnet from the Baoshan deposit.

Compared to the Eu^{3+} or the other REE^{3+} , Eu^{2+} can be incorporated into the scheelite directly due to having the same charge as Ca^{2+} . The Eu_N vs. δEu diagrams can well

distinguish the ionic valences of Eu in scheelite (Figure 16a) [56]. Eu^{3+} and Eu^{2+} can be identified by the data array with a slope of one or not, respectively. Sch I is characterized by moderate Eu_N^* and weak Eu anomalies with all points falling on the 1:1 correlation line, indicating that Eu^{3+} is dominant and Sch I precipitated from an oxidized hydrothermal fluid. The feature of Sch II is not similar to Sch I with a relatively lower $\text{Eu}_N/\delta\text{Eu}$ ratio and it diverges from the slope of one, which suggests a relative Eu^{2+} -dominant fluid and weak oxidized conditions. Sch I and Sch II from Line 153 exhibit similar trends with relatively lower $\text{Eu}_N/\delta\text{Eu}$ ratios, implying that they precipitated in a more reduced environment (Figure 16a). Compared to Sch I and Sch II, Sch III features significant high Eu_N^* characteristics with a strong correlation between Eu_N and δEu , which indicates that Eu^{3+} is dominant in the hydrothermal fluid. However, there was significantly negative Eu anomalies of Sch III in the deeper parts (Figure 16c), indicating Sch III was probably inherited from the hydrothermal fluid. No evidence indicates the existence of the pH transformation or the precipitation of the Eu-rich minerals, which are considered as the other factors controlling the Eu [58], due to the similar Eu anomalies during precipitation of the Sch I and Sch II and weak negative Eu anomalies of garnet at the Baoshan deposit (Figure 16c).

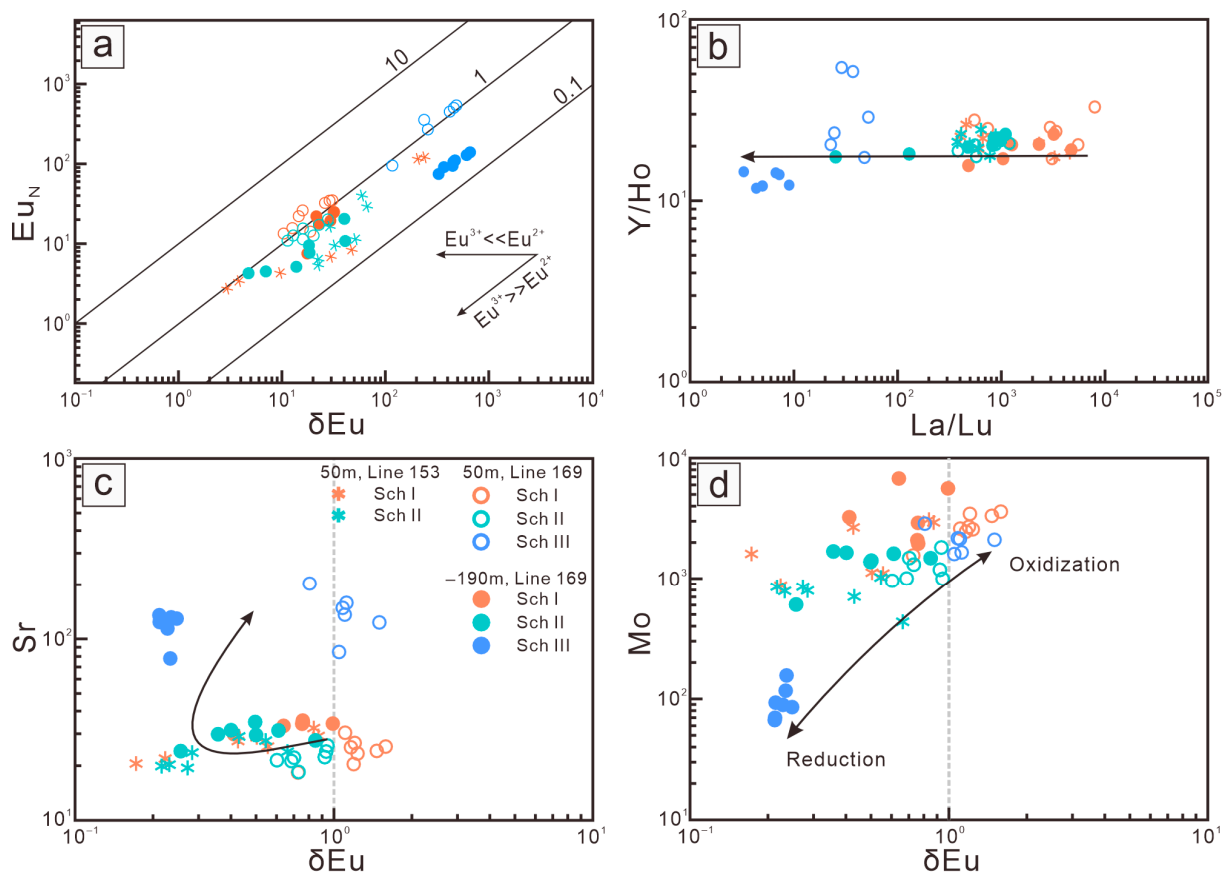


Figure 16. (a) Eu_N vs. δEu diagram, (b) Y/Ho vs. La/Lu diagram, (c) Sr vs. δEu diagram, and (d) Mo vs. δEu diagram for different types of scheelite from the Baoshan deposit. $\text{Eu}_N = \text{Eu}_{\text{sample}}/\text{Eu}_{\text{chondrite}}$; $\delta\text{Eu} = \text{Eu}_N/(\text{Sm}_N/\text{Nd}_N)^{1/2}$. Chondrite values according to the literature [55].

As mentioned above, as a redox-sensitive element, Mo is commonly used to identify redox conditions [2] and is favored to enter scheelite as Mo^{6+} under oxidizing conditions or precipitated as molybdenite under reducing conditions. The gradual decrease in concentration of Mo during the formation of Sch I and Sch II, implying a progressive decrease in oxidation conditions (Figure 16d), is consistent with the result of Eu. However, the

sharp decrease in Mo concentration in the deeper Sch III indicates a significant reduction in oxygen fugacity at depth (Figure 16d).

5.3. Sources and Evolution of Ore-Forming Fluids

In skarn deposits, the end-member compositions of garnet and pyroxene can be used to identify the types of ore-forming metals [21]. The garnet and pyroxene from the Baoshan Cu-polymetallic deposit mostly fall within the range typical for skarn Cu deposits (Figure 10a,b). Their compositions differ significantly from those found in typical skarn Sn, Mo, and Zn deposits (Figure 10a,b), suggesting that there may not be an overprint of a Sn polymetallic mineralization system in the Baoshan deposit. This is consistent with the macroscopic mineralogical characteristics, which lack cassiterite and stannite. In the late skarn stage, the first two generations of the scheelite (Sch I and Sch II) and shallow Sch III were identified to be skarn-type scheelite (Figure 17a,b), whereas deep Sch III was suggested to be a vein-type scheelite (Figure 17a,b).

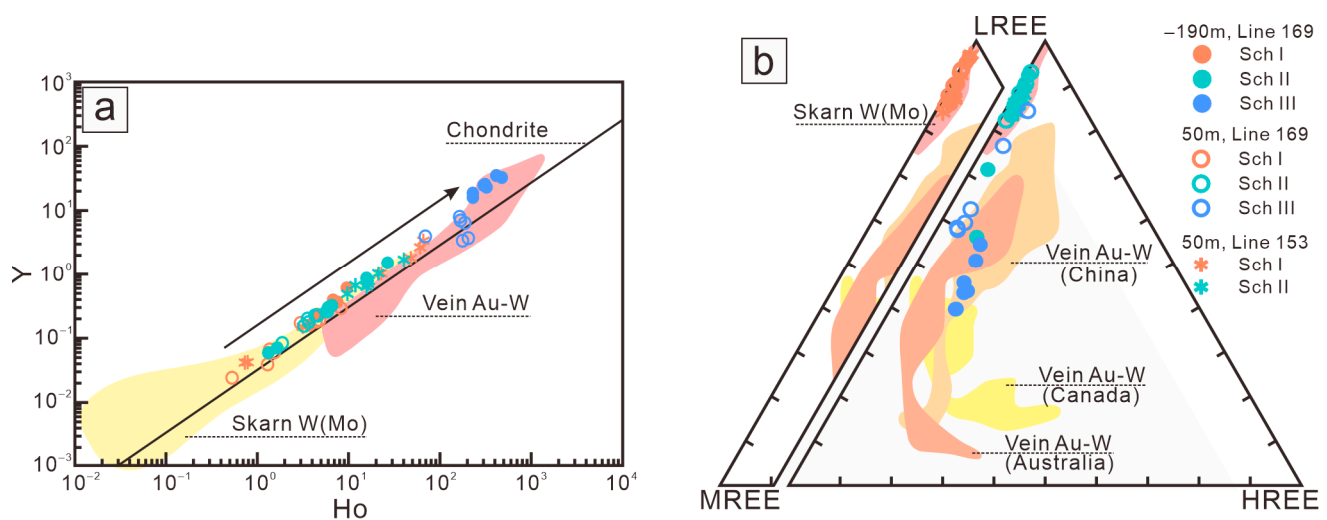


Figure 17. (a) Y vs. Ho diagram and (b) LREE-MREE-HREE diagram for scheelite from the Baoshan deposit. After Ding et al. [62].

The REE distribution pattern of garnet can effectively reflect the pH conditions of the mineralizing fluid. Garnet formed under near-neutral conditions typically exhibits an REE distribution pattern characterized by enrichment in HREE, depletion in LREE, and a negative or absent Eu anomaly. Garnet formed under weakly acidic conditions has an REE distribution pattern more controlled by Cl^- ions in the fluid, with Eu present as EuCl_4^{2-} , enhancing the stability of Eu^{2+} in the fluid and leading to a positive Eu anomaly in garnet [17,63]. The REE distribution patterns of the two generations of garnet in the Baoshan deposit are similar, showing relative enrichment of LREE, depletion of HREE, and weak negative or absent Eu anomalies (Figure 11a,b). This indicates that during the early skarn stage, when garnet formed, the mineralizing hydrothermal fluid was weakly acidic in pH.

The narrower Y/Ho ratios of Sch I, Sch II, and Sch III indicate that they may precipitate in a single fluid (Figure 16b). As mentioned above, the scheelite from the Baoshan deposit may preserve the REE pattern of the ore-forming fluid owing to its substitution mechanisms. The REE pattern of granodiorite porphyry is similar to those of Sch I and Sch II, exhibiting in a right-dip appearance, which indicates that Sch I and Sch II may be crystallized from the magmatic hydrothermal fluid associated with the granodiorite porphyry (Figure 13c) [64]. On the contrary, the hump-shaped REE pattern in Sch III and its independence from the Na-REE coupled substitution, as well as the congruent variation of LREE between Sch III and garnet (Figures 11a,b and 12c), suggest that remobilization of REE from the garnet may be inherited by Sch III. High concentration of Sr in scheelite can be attributed to fluid–rock

interactions [65,66] and the mixing with meteoric water [67]. Sch III should have been expected to obtain more Sr and a wide range of variation in Eu during the fluid–rock reactions with the limestone of the Shidengzi Formation due to its high Sr and low Eu characteristics (Figure 16c) [57,66]. The relatively stable Y/Ho ratio from Sch I to Sch III indicates that the increase in Sr content is not due to the addition of meteoric water. The increase in Sr content in Sch III may be related to water–rock interactions.

6. Conclusions

- (1) In the early skarn stage of the Baoshan deposit, two generations of garnet (Grt1 and Grt2) were identified, with Grt1 having a coarse granular texture and distinct zonation, and Grt2 cutting across Grt1 as veinlets. Additionally, pyroxene in the early skarn stage coexists with Grt1 and is similarly cut by Grt2. In the late skarn stage, three generations of scheelite (Sch I, Sch II, and Sch III) were identified. Sch I and Sch II appear as anhedral to subhedral grains, while Sch III is predominantly found in veinlets.
- (2) In Sch I and Sch II, most of the REEs enter the scheelite lattice via the Na-REE coupled substitution mechanism, with a smaller portion entering by substituting Ca vacancies. In Sch III, the substitution mechanism involving Ca site vacancies may dominate.
- (3) During the early skarn stage, the oxygen fugacity of the fluid gradually decreased from Grt1 and pyroxene to Grt2. During the late skarn stage, the fluid oxygen fugacity shows little change from Sch I and Sch II to Sch III in the shallow part, while it significantly decreases from Sch I and Sch II to Sch III in the deeper part.
- (4) The garnet and pyroxene from the Baoshan deposit align with typical skarn Cu deposit compositions, while scheelite in the late skarn stage shows Sch I, Sch II, and shallow Sch III as skarn-type and deep Sch III as vein-type scheelite. In the early skarn stage, the pH of the ore-forming hydrothermal fluid was weakly acidic. Sch I, Sch II, and Sch III originated from the magmatic hydrothermal fluids related to the Baoshan granite porphyry. The formation of Sch III also involved water–rock interactions.

Supplementary Materials: The following supporting information can be downloaded at: <https://www.mdpi.com/article/10.3390/min14090907/s1>. Table S1: The major element characteristics of garnet in Baoshan Cu-polymetallic deposit; Table S2: The trace element characteristics of garnet in Baoshan Cu-polymetallic deposit; Table S3: The major element characteristics of pyroxene in Baoshan Cu-polymetallic deposit; Table S4: LA-ICP-MS Data of Scheelite from the Baoshan Deposit.

Author Contributions: Conceptualization, P.Z. and K.C.; methodology, J.-K.Z.; software, J.-K.Z.; validation, Z.-F.L. and K.C.; formal analysis, M.-P.H.; investigation, J.-K.Z.; resources, Z.-F.L.; data curation, Y.-S.L.; writing—original draft preparation, P.Z.; writing—review and editing, K.C. and J.-K.Z.; visualization, Z.-F.L.; supervision, Y.-S.L.; project administration, K.C.; funding acquisition, P.Z. All authors have read and agreed to the published version of the manuscript.

Funding: This research was funded by the Key Laboratory Project of Metallogenic Prediction of Nonferrous Metals and Geological Environment Monitoring, Ministry of Education (Project number: 2023YSJS02); Hunan Provincial Department of Education Scientific Research Project (Project number: 22C0830); "Chu Yi" High level Teacher Team Construction Project of 2022 Vocational Education in Hunan Province.

Data Availability Statement: Data are contained within the Supplementary Materials and article.

Conflicts of Interest: All authors (Ping Zheng, Ke Chen, Jun-Ke Zhang, Zhong-Fa Liu, Yong-shun Li, and Ming-peng He) declare that they have no financial and personal relationships with other people or organizations that can inappropriately influence their work. There is no professional or other personal interest of any nature or kind in any product, service, or company that could be construed as influencing the position presented in, or the review of, the manuscript entitled.

References

1. Brugger, J.; Etschmann, B.; Pownceby, M.; Liu, W.; Grundler, P.; Brewster, D. Oxidation state of europium in scheelite: Tracking fluid–rock interaction in gold deposits. *Chem. Geol.* **2008**, *257*, 26–33. [[CrossRef](#)]

2. Fu, Y.; Hollings, P.; Li, D.; Liu, Q.; Li, S.; Sun, X. Geochemistry of multi-stage scheelite in the skarn: Constraints on ore-forming processes of the Machangqing Cu-Mo polymetallic deposit in Yunnan Province, southwest China. *Ore Geol. Rev.* **2021**, *138*, 104370. [[CrossRef](#)]
3. Han, J.; Chen, H.; Hong, W.; Hollings, P.; Chu, G.; Zhang, L.; Sun, S. Texture and geochemistry of multi-stage hydrothermal scheelite in the Tongshankou porphyry-skarn Cu-Mo (-W) deposit, eastern China: Implications for ore-forming process and fluid metasomatism. *Am. Mineral.* **2020**, *105*, 945–954. [[CrossRef](#)]
4. Song, G.; Cook, N.J.; Li, G.; Qin, K.; Ciobanu, C.L.; Yang, Y.; Xu, Y. Scheelite geochemistry in porphyry-skarn W-Mo systems: A case study from the Gaojiabang Deposit, East China. *Ore Geol. Rev.* **2019**, *113*, 103084. [[CrossRef](#)]
5. Yuan, L.; Chi, G.; Wang, M.; Li, Z.; Xu, D.; Deng, T.; Geng, J.; Hu, M.; Zhang, L. Characteristics of REEs and trace elements in scheelite from the Zhuxi W deposit, South China: Implications for the ore-forming conditions and processes. *Ore Geol. Rev.* **2019**, *109*, 585–597. [[CrossRef](#)]
6. Li, W.; Xie, G.-Q.; Mao, J.-W.; Zhang, H.-C. Mineralogy, fluid inclusion and isotope signatures: Implications for the genesis of the Early Paleozoic Yangjiashan scheelite-quartz vein deposit, South China. *Ore Geol. Rev.* **2021**, *134*, 104136. [[CrossRef](#)]
7. Orhan, A. Evolution of the Mo-rich scheelite skarn mineralization at Kozbudaklar, Western Anatolia, Turkey: Evidence from mineral chemistry and fluid inclusions. *Ore Geol. Rev.* **2017**, *80*, 141–165. [[CrossRef](#)]
8. Singoyi, B.; Zaw, K. A petrological and fluid inclusion study of magnetite–scheelite skarn mineralization at Kara, Northwestern Tasmania: Implications for ore genesis. *Chem. Geol.* **2001**, *173*, 239–253. [[CrossRef](#)]
9. Bell, K.; Anglin, C.; Franklin, J. Sm-Nd and Rb-Sr isotope systematics of scheelites: Possible implications for the age and genesis of vein-hosted gold deposits. *Geology* **1989**, *17*, 500–504. [[CrossRef](#)]
10. Guo, Z.; Li, J.; Xu, X.; Song, Z.; Dong, X.; Tian, J.; Yang, Y.; She, H.; Xiang, A.; Kang, Y. Sm-Nd dating and REE Composition of scheelite for the Honghuaerji scheelite deposit, Inner Mongolia, Northeast China. *Lithos* **2016**, *261*, 307–321. [[CrossRef](#)]
11. Palmer, M.C.; Scott, J.M.; Luo, Y.; Sakar, C.; Pearson, D.G. In-situ scheelite LASS-ICPMS reconnaissance Sm-Nd isotope characterisation and prospects for dating. *J. Geochem. Explor.* **2021**, *224*, 106760. [[CrossRef](#)]
12. Scanlan, E.J.; Scott, J.M.; Wilson, V.J.; Stirling, C.H.; Reid, M.R.; Le Roux, P.J. In situ $^{87}\text{Sr}/^{86}\text{Sr}$ of scheelite and calcite reveals proximal and distal fluid-rock interaction during orogenic W-Au mineralization, Otago Schist, New Zealand. *Econ. Geol.* **2018**, *113*, 1571–1586. [[CrossRef](#)]
13. Song, G.; Qin, K.; Li, G.; Evans, N.J.; Chen, L. Scheelite elemental and isotopic signatures: Implications for the genesis of skarn-type W-Mo deposits in the Chizhou Area, Anhui Province, Eastern China. *Am. Mineral.* **2014**, *99*, 303–317. [[CrossRef](#)]
14. Sun, K.; Chen, B. Trace elements and Sr-Nd isotopes of scheelite: Implications for the W-Cu-Mo polymetallic mineralization of the Shimensi deposit, South China. *Am. Mineral.* **2017**, *102*, 1114–1128.
15. Poulin, R.S.; Kontak, D.J.; McDonald, A.; Mcclenaghan, M.B. Assessing scheelite as an ore-deposit discriminator using its trace-element and REE chemistry. *Can. Mineral.* **2018**, *56*, 265–302. [[CrossRef](#)]
16. Sciuba, M.; Beaudoin, G.; Grzela, D.; Makvandi, S. Trace element composition of scheelite in orogenic gold deposits. *Miner. Depos.* **2020**, *55*, 1149–1172. [[CrossRef](#)]
17. Gaspar, M.; Knaack, C.; Meinert, L.D.; Moretti, R. REE in skarn systems: A LA-ICP-MS study of garnets from the Crown Jewel gold deposit. *Geochim. Cosmochim. Acta* **2008**, *72*, 185–205. [[CrossRef](#)]
18. Ague, J.J.; Carlson, W.D. Metamorphism as garnet sees it: The kinetics of nucleation and growth, equilibration, and diffusional relaxation. *Elements* **2013**, *9*, 439–445. [[CrossRef](#)]
19. Bian, X.L.; Zhang, J.; Wang, J.L.; Liu, C.F.; Yu, H.J. In situ analysis of garnets from the Hongshan skarn copper deposit in Northwest Yunnan Province and its geological implications. *Acta Petrol. Sin.* **2019**, *35*, 1463–1477. (In Chinese with English Abstract)
20. Meinert, L.D. Skarns and skarn deposits. *Geosci. Can.* **1992**, *19*, 145–162.
21. Meinert, L.D. Compositional variation of igneous rocks associated with skarn deposits—chemical evidence for a genetic connection between petrogenesis and mineralization. *Mineral. Assoc. Can. Short Course Ser.* **1995**, *23*, 401–418.
22. Chen, K.; Shao, Y.J.; Zhang, J.K.; Zhang, Y.; Tan, H.J.; Zhang, Y.C.; Liu, Z.F. Garnet U-Pb geochronology and geochemistry reveal deposit types and fluid evolution: An example from the Dongguashan Cu-Au deposit, eastern China. *Ore Geol. Rev.* **2022**, *145*, 104883. [[CrossRef](#)]
23. Yu, F.; Shu, Q.; Niu, X.; Xing, K.; Li, L.; Lentz, D.R.; Zeng, Q.; Yang, W. Composition of garnet from the Xianghualing Skarn Sn Deposit, South China: Its petrogenetic significance and exploration potential. *Minerals* **2020**, *10*, 456. [[CrossRef](#)]
24. Duan, X.X.; Ju, Y.F.; Chen, B.; Wang, Z.Q. Garnet Geochemistry of Reduced Skarn System: Implications for Fluid Evolution and Skarn Formation of the Zhuxiling W (Mo) Deposit, China. *Minerals* **2020**, *10*, 1024. [[CrossRef](#)]
25. Ding, T.; Tan, T.T.; Wang, J.; Ma, D.S.; Lu, J.J.; Zhang, R.Q.; Liang, J. Trace-element composition of pyrite in the Baoshan Cu-Mo-Pb-Zn deposit, southern Hunan Province, China: Insights into the ore genesis. *Ore Geol. Rev.* **2022**, *147*, 104989. [[CrossRef](#)]
26. Ding, T.; Tan, T.; Wang, J.; Ma, D.; Lu, J.; Zhang, R.; Liang, J.; Wu, B. Multiple sources for the Baoshan polymetallic Cu-Mo-Pb-Zn deposit, southern Hunan Province, China: Insights from in situ LA-MC-ICP-MS sulfur isotopic compositions. *Ore Geol. Rev.* **2022**, *143*, 104808. [[CrossRef](#)]
27. Hu, T.Y.; Liu, L.; Zhou, W.J.; Shao, Y.J.; Li, H.; Liu, Z.F.; Cao, L.; Xu, G.F.; Li, J.X. Contributions of trans-magmatic fluid in the formation of porphyry copper deposits: A case study from the Baoshan deposit, South China. *Geochemistry* **2022**, *82*, 125881. [[CrossRef](#)]

28. Huang, W.T.; Liang, H.Y.; Zhang, J.; Wu, J.; Chen, X.L.; Ren, L. Genesis of the Dachang Sn-polymetallic and Baoshan Cu ore deposits, and formation of a Cretaceous Sn-Cu ore belt from southwest China to western Myanmar. *Ore Geol. Rev.* **2019**, *112*, 103030. [[CrossRef](#)]
29. Ren, L.; Sun, J.; Han, J.; Liu, Y.; Wang, C.; Gu, A.; Zhao, K.; Yu, R. Magmatism and metallogenic mechanisms of the Baoshan Cu-polymetallic deposit from the Lesser Xing'an Range, NE China: Constraints from geology, geochronology, geochemistry, and Hf isotopes. *Ore Geol. Rev.* **2017**, *88*, 270–288. [[CrossRef](#)]
30. Xie, Y.C.; Lu, J.J.; Yang, P.; Ma, D.S.; Xu, Z.W.; Zhang, R.Q.; Cai, Y.; Ding, T. S, Pb, C and O isotopic characteristics and sources of metallogenic materials of Baoshan Pb–Zn deposit, southern Huanan Province. *Miner. Depos.* **2015**, *34*, 333–351.
31. Xie, Y.C.; Lu, J.J.; Ma, D.S.; Zhang, R.Q.; Gao, J.F.; Yao, Y. Origin of granodiorite porphyry and mafic microgranular enclave in the Baoshan Pb–Zn polymetallic deposit, southern Hunan Province: Zircon U–Pb chronological, geochemical and Sr–Nd–Hf isotopic constraints. *Acta Petrol. Sin.* **2013**, *29*, 4186–4214.
32. Zhang, J.K.; Shao, Y.J.; Chen, K.; Tan, H.J.; Tan, R.C.; Zhang, T.D.; Liu, Z.F. Evidence of fluid evolution of Baoshan Cu–Pb–Zn polymetallic deposit: Constraints from in-situ sulfur isotope and trace element compositions of pyrite. *Trans. Nonferrous Met. Soc. China* **2021**, *31*, 3530–3548. [[CrossRef](#)]
33. Zhao, W.W.; Zhou, M.-F. Mineralogical and metasomatic evolution of the Jurassic Baoshan scheelite skarn deposit, Nanling, South China. *Ore Geol. Rev.* **2018**, *95*, 182–194. [[CrossRef](#)]
34. Mao, J.W.; Chen, M.H.; Yuan, S.D.; Guo, C.L. Geological Characteristics of the Qinhang (or Shihang) Metallogenic Belt in South China and Spatia-l Temporal Distribution Regularity of Mineral Deposits. *Acta Geol. Sin.* **2011**, *85*, 636–658. (In Chinese with English Abstract)
35. Kong, H.; Li, H.; Wu, Q.H.; Xi, X.S.; Dick, J.M.; Gabo-Ratio, J.a.S. Co-development of Jurassic I-type and A-type granites in southern Hunan, South China: Dual control by plate subduction and intraplate mantle upwelling. *Geochemistry* **2018**, *78*, 500–520. [[CrossRef](#)]
36. Zhou, X.M.; Sun, T.; Shen, W.Z.; Shu, L.S.; Niu, Y.L. Petrogenesis of Mesozoic granitoids and volcanic rocks in South China: A response to tectonic evolution. *Episodes* **2006**, *29*, 26–33. [[CrossRef](#)]
37. Mi, J.R.; Yuan, S.D.; Xuan, Y.S.; Zhang, D.L. Zircon U–Pb ages, Hf isotope and trace element characteristics of the granodiorite porphyry from the Baoshan–Dafang ore district, Hunan: Implications for regional metallogeny. *Acta Petrol. Sin.* **2018**, *34*, 2548–2564.
38. Zhao, P.L.; Yuan, S.D.; Mao, J.W.; Santosh, M.; Zhang, D.L. Zircon U–Pb and Hf–O isotopes trace the architecture of polymetallic deposits: A case study of the Jurassic ore-forming porphyries in the Qin–Hang metallogenic belt, China. *Lithos* **2017**, *292*, 132–145. [[CrossRef](#)]
39. Hacker, B.R.; Ratschbacher, L.; Webb, L.; Ireland, T.; Walker, D.; Shuwen, D. U/Pb zircon ages constrain the architecture of the ultrahigh-pressure Qinling–Dabie Orogen, China. *Earth Planet. Sci. Lett.* **1998**, *161*, 215–230. [[CrossRef](#)]
40. Cawood, P.A. Terra Australis Orogen: Rodinia breakup and development of the Pacific and Iapetus margins of Gondwana during the Neoproterozoic and Paleozoic. *Earth-Sci. Rev.* **2005**, *69*, 249–279. [[CrossRef](#)]
41. Fan, W.; Wang, Y.; Zhang, A.; Zhang, F.; Zhang, Y. Permian arc–back–arc basin development along the Ailaoshan tectonic zone: Geochemical, isotopic and geochronological evidence from the Mojiang volcanic rocks, Southwest China. *Lithos* **2010**, *119*, 553–568. [[CrossRef](#)]
42. Zhang, Y.Q.; Xu, X.B.; Jia, D.; Shu, L.S. Deformation record of the change from Indosinian collision-related tectonic system to Yanshanian subduction-related tectonic system in South China during the Early Mesozoic. *Earth Sci. Front.* **2009**, *16*, 234–247. (In Chinese with English abstract)
43. Li, D.F.; Tan, C.Y.; Miao, F.Y.; Liu, Q.F.; Zhang, Y.; Sun, X.M. Initiation of Zn–Pb mineralization in the Pingbao Pb–Zn skarn district, South China: Constraints from U–Pb dating of grossular-rich garnet. *Ore Geol. Rev.* **2019**, *107*, 587–599. [[CrossRef](#)]
44. Hou, Z.Q.; Pan, X.F.; Li, Q.Y.; Yang, Z.M.; Song, Y.C. The giant Dexing porphyry Cu–Mo–Au deposit in east China: Product of melting of juvenile lower crust in an intracontinental setting. *Miner. Depos.* **2013**, *48*, 1019–1045. [[CrossRef](#)]
45. Hou, Z.Q.; Yang, Z.M.; Wang, R.; Zheng, Y.C. Further discussion on porphyry Cu–Mo–Au deposit formation in Chinese mainland. *Earth Sci. Front. (China Univ. Geosci. Beijing)* **2020**, *27*, 020–044. (In Chinese with English Abstract)
46. Hua, R.M.; Chen, P.R.; Zhang, W.L.; Yao, J.M.; Lin, J.F.; Zhang, Z.S.; Gu, S.Y. Metallogenesis and Their Geodynamic Settings Related to Mesozoic Granitoids in the Nanling Range. *Geol. J. China Univ.* **2005**, *11*, 291. (In Chinese with English Abstract)
47. Zhao, Z.H.; Bao, Z.W.; Zhang, B.Y. Geochemistry of the Mesozoic basaltic rocks in southern Hunan Province. *Sci. China Ser. D Earth Sci.* **1998**, *41*, 102–112. [[CrossRef](#)]
48. Kong, H.; Quan, T.J.; Xi, X.S.; Zhong, J.L.; Chen, Z.F.; Wang, G.; Guo, B.Y.; Zhao, Z.Q. Geochemical characteristics of lamprophyre and its geological significance in Baoshan deposit, Hunan province, China. *Chin. J. Nonferrous Met.* **2013**, *23*, 2671–2682. (In Chinese with English Abstract)
49. Lu, Y.F.; Ma, L.Y.; Qu, W.J.; Mel, Y.P.; Chen, X.Q. U–Pb and Re–Os isotope geochronology of Baoshan Cu–Mo polymetallic ore deposit in Hunan province. *Acta Petrol. Sin.* **2006**, *22*, 2483–2492. (In Chinese with English Abstract)
50. Zhang, J.K.; Shao, Y.J.; Liu, Z.F.; Chen, K. Sphalerite as a record of metallogenic information using multivariate statistical analysis: Constraints from trace element geochemistry. *J. Geochem. Explor.* **2022**, *232*, 106883. [[CrossRef](#)]
51. Li, H.; Kong, H.; Zhou, Z.-K.; Wu, Q.-H.; Xi, X.-S.; Gabo-Ratio, J.a.S. Ore-forming material sources of the Jurassic Cu–Pb–Zn mineralization in the Qin–Hang ore belt, South China: Constraints from S–Pb isotopes. *Geochemistry* **2019**, *79*, 280–306. [[CrossRef](#)]

52. Reed, W.P. *Certificate of Analysis: Standard Reference Materials 610 and 611*; National Institute of Standards and Technology: Gaithersburg, MD, USA, 1992.
53. Liu, Y.S.; Hu, Z.C.; Shan, G.; Günther, D.; Xu, J. In situ analysis of major and trace elements of anhydrous minerals by LA-ICP-MS without applying an internal standard. *Chem. Geol.* **2008**, *257*, 34–43. [[CrossRef](#)]
54. Meinert, L.D. World skarn deposits. In *Economic Geology 100th Anniversary Volume*; Society of Economic Geologists, Inc.: Littleton, Co, USA, 2005; pp. 236–299.
55. Sun, S.S.; McDonough, W.F. Chemical and isotopic systematics of oceanic basalts: Implications for mantle composition and processes. *Geol. Soc. Lond. Spec. Publ.* **1989**, *42*, 313–345. [[CrossRef](#)]
56. Ghaderi, M.; Palin, J.M.; Campbell, I.H.; Sylvester, P.J. Rare earth element systematics in scheelite from hydrothermal gold deposits in the Kalgoorlie-Norseman region, Western Australia. *Econ. Geol.* **1999**, *94*, 423–437. [[CrossRef](#)]
57. Yao, J.M.; Hua, R.M.; Lin, J.F. REE, Pb-S Isotope Geochemistry, and Rb-Sr Isochron Age of Pyrites in the Baoshan Deposit, South Hunan Province, China. *Acta Geol. Sin.* **2006**, *80*, 1045–1054. (In Chinese with English Abstract)
58. Zhan, Q.; Gao, X.-Y.; Meng, L.; Zhao, T.-P. Ore genesis and fluid evolution of the Sandaozhuang supergiant W-Mo skarn deposit, southern margin of the North China Craton: Insights from scheelite, garnet and clinopyroxene geochemistry. *Ore Geol. Rev.* **2021**, *139*, 104551. [[CrossRef](#)]
59. Li, S.T. Characteristics and Genesis of the Yaogangxian Tungsten Polymetallic Deposits in Hunan Province. Ph.D. Thesis, China University of Geosciences (Beijing), Beijing, China, 2011. (In Chinese with English Abstract)
60. Feng, C.Y.; Wang, S.; Li, G.C.; Ma, S.C.; Li, D.S. Middle to Late Triassic granitoids in the Qimantage area, Qinghai Province, China: Chronology, geochemistry and metallogenic significances. *Acta Petrol. Sin.* **2012**, *28*, 665–678. (In Chinese with English Abstract)
61. Zhang, R.Q. Petrogenesis and Metallogeny of the W- and Sn-Bearing Granites in Southern Hunan Province: Case Study from Wangxianling and Xintianling. Ph.D. Thesis, Nanjing University, Nanjing, China, 2015. (In Chinese with English Abstract)
62. Ding, T.; Ma, D.S.; Lu, J.J.; Zhang, R.Q. Garnet and scheelite as indicators of multi-stage tungsten mineralization in the Huangshaping deposit, southern Hunan province, China. *Ore Geol. Rev.* **2018**, *94*, 193–211. [[CrossRef](#)]
63. Zhao, L.J.; Zhang, Y.; Shao, Y.J.; Li, H.B.; Shah, S.A.; Zhou, W.J. Using garnet geochemistry discriminating different skarn mineralization systems: Perspective from Huangshaping W-Mo-Sn-Cu polymetallic deposit, South China. *Ore Geol. Rev.* **2021**, *138*, 104412. [[CrossRef](#)]
64. Zhang, D.; Pan, J.; Gao, J.; Dai, T.; Bayless, R.C. In situ LA ICP-MS analysis of trace elements in scheelite from the Xuefeng Uplift Belt, South China and its metallogenic implications. *Ore Geol. Rev.* **2021**, *133*, 104097. [[CrossRef](#)]
65. Qi, H.; Yang, X.; Lu, S.; Tang, C.; Cao, J.; Zhao, L.; Deng, J.; Sun, C.; Zhao, Z.; Lee, I. Ore genesis and fluid evolution of the Qiaomaishan Cu–W deposit, in the Middle-Lower Yangtze River Metallogenic Belt: Evidence from in situ analyses of apatite and scheelite. *Ore Geol. Rev.* **2020**, *127*, 103864. [[CrossRef](#)]
66. Sun, K.; Chen, B.; Deng, J. Ore genesis of the Zhuxi supergiant W-Cu skarn polymetallic deposit, South China: Evidence from scheelite geochemistry. *Ore Geol. Rev.* **2019**, *107*, 14–29. [[CrossRef](#)]
67. Zhang, Y.; Ma, D.; Gao, J.-F. Origin and evolution of ore-forming fluids in a tungsten mineralization system, Middle Jiangnan orogenic belt, South China: Constraints from in-situ LA-ICP-MS analyses of scheelite. *Ore Geol. Rev.* **2020**, *127*, 103806. [[CrossRef](#)]

Disclaimer/Publisher’s Note: The statements, opinions and data contained in all publications are solely those of the individual author(s) and contributor(s) and not of MDPI and/or the editor(s). MDPI and/or the editor(s) disclaim responsibility for any injury to people or property resulting from any ideas, methods, instructions or products referred to in the content.